59115

Technical Report for NASA grant C036846 (NAG3-2134),

R.G. Larson, P.I., July 25, 2002

In this report, we summarize work carried out under the above-named grant, primarily by post-doc Hua Hu, and partially by grad students Lei Li and Manish Chopra. The work includes studies on droplet evaporation and its effects on temperature and velocity fields in an evaporating droplet, new 3-D microscopic particle image velocimetry and direct visualization on wall slip in a surfactant solution. With the exception of the slip measurements, these projects were those proposed in the grant application. Instead of slip flow, the original grant proposed imaging electro-osmotic flows. However, shortly after the grant was issued, the PI became aware of work on electro-osmotic flows by the group of Saville in Princeton that was similar to that proposed, and we therefore elected to carry out work on imaging slip flows rather than electro-osmotic flows. The following paragraphs are the detailed descriptions on these projects.

1. Droplet evaporation

The evaporation of a sessile droplet with a pinned contact line was investigated by experiments, by analytic theory, and by computation using the finite element method (FEM). We compared the results obtained by our FEM analysis with an analytical solution and derived a very simple approximate evaporation rate expression $\dot{m}(t) = -\pi\, RD(1-H)c_v(0.27\theta^2 + 1.30)$ for any initial contact angle _ between 0 and _/2 with _ in radians. The approximate expression was also compared with droplet evaporation data from the literature, and good agreement found without any parameter fitting. It was found both theoretically and experimentally that the net evaporation rate from the droplet remained almost constant with time for a small initial contact angle ($\theta <$ 40°), even though the evaporation flux becomes more strongly singular at the edge of the droplet as the contact angle decreases during evaporation. The results of this study were applied almost immediately by the group of Kate Stebe at Johns Hopkins University, who found that the above formula applies even when evaporation is strongly suppressed by a

surfactant-monoloayer covering the droplet, as long as the droplet does not become too small

Key Result: A simple and accurate formula for predicting the contact-angle dependence of the evaporation rate from a sessile droplet, which has been used by Prof. Stebe at Johns Hopkins in research on monolayer-covered droplets.

2. Temperature and velocity fields in the evaporating droplet

With the results of the droplet evaporation, we used FEM analysis to compute the temperature field in the evaporating droplet. We found that the temperature field varies with the contact angle and the surface temperature becomes non-uniform along the droplet surface. We believe a surface-tension gradient generated by this non-uniform temperature distribution produces a Marangoni flow in the droplet.

Thus, the 3-D time-dependent flow field produced by the evaporating droplet was studied theoretically and experimentally. We developed an analytic lubrication theory for this flow in the evaporating droplet both with and without Marangoni stresses. Since the most available commercial software doesn't allow us to solve a moving boundary problem with Marangoni stress, we developed our own FEM code to solve the Stokes equation in the evaporating droplet. The FEM results confirmed the validity and accuracy of our approximate analytic solutions for flow field in the droplet. We found that large thermally-induced Marangoni flows are predicted for evaporation of pure water, but that these Marangoni flows are severely attenuated in the experiments, evidently due to trace contaminants producing an offsetting Marangoni stress due to surface-active agents. Defocused particle-tracking velocimetry is presented and applied to map the 3-dimensional time-dependent particle displacements. The measured velocity field shows that there is a weak recirculation near the droplet surface, evidently due to Marangoni stresses produced by temperature gradients arising from evaporation.

Key Result: An analytic lubrication analysis of the entire 3D flow field in an evaporating droplet, including the effects of Marangoni flow, with verification of the accuracy of the analytic analysis using full FEM, including effects of evaporative

cooling. This result was recently used to predict DNA deposition from an evaporating droplet, a technique used by the David Schwartz group in Wisconsin for genomic mapping, including mapping the genome of the parasite *plasmodium* that causes malaria.

3. Microscopic 3-D PIV

In order to map the micro-fluidic flow, we developed two microscopic versions of particle image velocimetry. For the flow in the evaporating droplet, 3-D microscopic particle-tracking technique was established. In our experiments, we observed particle ring patterns, from which we can extract the vertical particle displacement. By tracking the particle, we were able for the first time to obtain the 3-dimesional-velocity field from a 2-dimensional particle image. Considering the differences between microscopic and macroscopic flow properties, we built our own microscopic PIV(particle-image-velocimetry) for general 2-D micro-fluidic system, which we then employed to study the wall-slip velocity in a surfactant solution.

Key Result: A new particle imaging velocimetry method that can be applied to microscopic flows and can extract three-dimensional velocities from two-dimensional images by using defocused images quantitatively.

4. Direct visualization of wall-slip in a surface solution

A microscope-mounted torsional shearing-flow cell was constructed and microscopic particle imaging velocimetry employed to directly visualize and map the velocity slip layer in a shearing flow of dilute micellar surfactant solutions of cetyltriammonium bromide/sodium salicylate. It was shown that the thickness of the wall-slip layer is about 100 mm at low shear rates, decreasing to around 50–60mm at high shear rates. Surprisingly, we found that the wall slip layer emerged only near the upper rotating plate of the flow cell, and not the lower surface, a phenomenon that is still unexplained. The rheological properties of the wormy micellar solutions were also measured by using a stress-controlled rheometer and the results compared to the visualization results of wall-slip velocity in the shearing-flow cell. Above the critical point, the shear viscosity reaches a plateau and decreases at a higher shear rate where we

observed that the flow becomes unstable. As the gap of parallel plate geometry or the cone angle of cone-plate geometry increased, the critical shear rate decreased, because the wall-slip layer formed in the flow cell even below the shear thickening transition. We extracted the wall-slip velocities from the rheological data using a Mooney analysis and show, apparently for the first time, that the slip velocity from the Mooney analysis is consistent with that obtained by direct visualization experiments.

Key Result: First direct verification that slip velocities extracted from macroscopic gap-dependent rheology measurements are consistent with direct microscopic measurements of slip, thus validating a 50-year-old technique, the Mooney analysis. Also, microscopic imaging of thick slip layers in flowing surfactant solutions.

Publications

Four papers have been generated through these studies. Two of them have been published and the other two are in preparation for submission. Attachments are the published papers and a preliminary, partial, report on micro-fluid dynamics. The latter does not yet contain a full write-up of the recently completed FEM study. The follow is a list of the papers arising from this grant:

- Hua Hu and R. G. Larson, Evaporation of a Sessile Droplet on a Substrate, J. Phys. Chem. B, 106, 1334-1344(2002).
- Hua Hu and R. G. Larson, J.J Magda, Measurement of wall-slip-layer rheology in shear-thickening wormy micelle solutions, J. Rheol. 46~4, 1001-1021(2002).
- Hu, H., Larson, R. G., Micro-Fluid Dynamics in an Evaporating Sessile Droplet, to be submitted.
- Chopra, M., Li, L., Hu, H., Burns, M.A., Larson, R.G. DNA Molecular Configurations in an Evaporating Droplet Near a Glass Surface, to be submitted (2002).

Evaporation of a Sessile Droplet on a Substrate

Hua Hu* and Ronald G. Larson

Department of Chem. Eng., University of Michigan, Ann Arbor, Michigan 48109-2136

Received: May 14, 2001; In Final Form: September 20, 2001

The evaporation of a sessile droplet with a pinned contact line is investigated experimentally, by analytic theory and by computation using the finite element method (FEM). Because of the low value of $R^2/Dt_f = c_v(1 - H)/\rho = 1.4 \times 10^{-5}$, where R is the contact-line radius, D is the water vapor diffusivity, c_v is the saturated water vapor concentration, H is the relative humidity, and ρ is the liquid water density, the evaporation can be considered as a quasi-steady-state process. Hence, the vapor concentration distribution above the droplet satisfies the Laplace equation but with a time-varying droplet surface. It is found both theoretically and experimentally that the net evaporation rate from the droplet remains almost constant with time for a small initial contact angle ($\theta < 40°$), even though the evaporation flux becomes more strongly singular at the edge of the droplet as the contact angle decreases during evaporation. We also measured the critical contact angle at which the contact line starts to recede and found that it is about 2−4° for clean water on glass. Finally, we compare the results obtained by our FEM analysis with an analytical solution and derive a very simple approximate evaporation rate expression $\dot{m}(t) = -\pi RD(1 - H)c_v(0.27\theta^2 + 1.30)$, which agrees with the theoretical results presented by Lebedev [Lebedev, N. N. *Special Functions and Their Application*; Prentice Hall: Englewood Cliffs, New Jersey, 1965 and Picknett and Bexon [Picknett, R. G.; Bexon, R. *J. Colloid Interface Sci.* 1977, 61, 366] for any initial contact angle θ between 0 and $\pi/2$ with θ in radians. The approximate expression is also compared with droplet evaporation data from the literature, and good agreement is found without any parameter fitting.

1. Introduction

The evaporation of a sessile droplet is not only important in many heat transfer applications but is associated with common, everyday phenomena, such as the annoying ring-like spots left on dishes that are allowed to dry. Recently, important new applications of this simple phenomenon have emerged. Jing and co-workers[1] have developed a high-throughput automatic DNA mapping method based on drying droplet. In this technique, water evaporation is used both to induce a microscopic flow that stretches DNA molecules and to deposit those molecules onto a substrate where they can be subjected to a restriction digestion. The locations of digestion sites along the DNA strand observed in an optical microscope then constitutes on "optical map" of the DNA molecule. Droplet drying is also important in the creation of arrays of DNA spots for gene expression analysis. Li et al.[2] found that the DNA's stretching behavior is strongly affected by the evaporation rate of droplet. At a low evaporation rate, the DNA molecules are less stretched and their molecular conformations are folded or coiled, whereas at a high evaporation rate, DNA molecules are more stretched and their shapes become dumbbells or half-dumbbells. Thus, there are new motivations for revisiting the old problem of a drying sessile droplet.

The evaporation of a sessile droplet has been studied by Birdi and Winter,[3] who obtained the evaporation rate by measuring the change of weight of droplets of water on a glass surface and concluded that for most of the time during the evaporation the evaporation rate remains constant. Later, they[4] reported that the rate of evaporation of sessile drops of water on glass (contact angle $\theta = 41°$) and n-octane on Teflon surfaces is constant in time with the contact line pinned. Shanahan and Bourges[5,6] investigated the evaporation of droplets of water from smooth polyethylene and from both smooth and rough epoxy resin surfaces. They measured the change of drop height, contact angle, and contact-line radius with time and observed that evaporation occurs in several distinct stages. In the longest of these, the droplet flattens as it evaporates with the contact line pinned. Rowan et al.[7,8] presented detailed measurements of the change in contact angle and height with time for water on poly(methyl methacrylate), PMMA, and for three alcohols resting on Teflon. Starting with a large initial contact angle ($\theta \approx 80°$), both the height and the contact angle decreased linearly with time.

Lebedev,[9] and later Picknett and Bexon,[10] independently, used the analogy between diffusive concentration fields and electrostatic potential fields (they both satisfy Laplace's equation) to the problem of evaporation of a sessile droplet. For diffusion-controlled evaporation, the vapor concentration field is equivalent to the electrostatic potential field around the top half of an equiconvex lens. These theoretical results should be valid as long as the sessile droplet remains in the shape of a spherical cap. Bourges and Shanahan[6] proposed an evaporation model for the sessile droplet by taking the concentration gradient to be that for a hemispherical droplet of same radius as that of the sessile droplet. This approximation is not accurate for a flat droplet because the distribution of the evaporation flux along a sessile droplet surface is not uniform as it would be for a hemispherical droplet. Rowan et al.[7] analyzed the problem theoretically using a vapor-phase diffusion model suggested by Birdi et al.[3] and derived an approximate analytic equation for the evaporation rate. Their model fits experimental results very well for droplets with large initial contact angle. Erbil et al.[11]

* To whom correspondence should be addressed.

10.1021/jp0118322 CCC: $22.00
Published on Web 01/18/2002

modeled the droplet as an ellipsoidal cap, defined by three parameters. By adjusting these parameters, they obtained good agreement with experiments. Meric and Erbil[12] reported another model considering a "pseudo-spherical-cap" geometry (for which the droplet height is given by $h_0 = \alpha R \tan \theta/2$, where R is the droplet radius and α is an adjustable flatness parameter, with $\alpha = 1$ for a spherical cap), which they argued provided much better fits to experimental results. Deegan et al.[13,14] presented an analytical solution for a droplet with the shape of a spherical cap. Although authors neglected the evaporation flux distribution along the droplet surface, Deegan et al.[14] used the exact analytic expression for the evaporation flux distribution derived by Lebedev.[9] However, Deegan et al. did not study the relationship between the evaporation rate or flux distribution and the contact angle. The purpose of this article is to develop a simple, yet accurate, model for evaporation of a small droplet with the shape of a spherical cap and to lay the basis for calculating the Marangoni force induced by a nonuniform distribution of the evaporation flux and for developing an accurate model for the complete flow field in an evaporating droplet, to be presented in a forthcoming paper.[15] This flow model will, in future work, be used for predicting stretching and deposition of DNA molecules in an evaporating droplet.

In this paper, we first use a finite element method to solve for the outer vapor concentration and evaporation flux. The evaporation flux distribution along the droplet surface is not uniform when a droplet is placed on the surface. The nonuniform evaporation flux eventually affects the droplet surface temperature distribution and therefore generates a surface tension gradient along the droplet surface, which may be a possible contributing factor for the contact-line pinning during evaporation. Second, we describe a particle-tracking method to measure the time-dependent change in droplet shape and the rate of droplet evaporation. Then the experimental results are presented and compared with the results computed by the FEM method. Finally, our model for the rate of the evaporation is compared to the results reported in the literature, and a simple, yet accurate, empirical expression for the evaporation rate as a function of contact angle is obtained. The empirical expression is also compared to the theoretical results derived by Lebedev[9] and Picknett and Bexon.[10]

2. Theory

From our experimental observations, we have found that, when the contact angle is less than 90°, droplet evaporation generally includes two main phases. In the first phase, the contact angle decreases while the contact line is pinned. In the second phase, the contact line recedes while the contact angle remains very small. Because the first phase occupies the 90–95% of the total drying time, we only consider this phase in which the contact line is pinned. In this section, we develop a mathematical model and a corresponding FEM solution for the droplet evaporation rate.

2.1. Mathematical Model. Here, we consider a sessile droplet having the shape of a spherical cap resting on a flat substrate. The droplet shape is controlled by the Bond number, $Bo = \rho g R h_0/\sigma$, which accounts for the balance of surface tension and gravitational force on the droplet shape, and the capillary number $Ca = \mu \bar{u}_r/\sigma$, which is the ratio of viscous to capillary forces. Here, ρ is the fluid density, g is the gravitational constant, R is the contact-line radius, h_0 is the initial height of the droplet, σ is the air–water surface tension, μ is the liquid viscosity, and $\bar{u}_r$ is the average radial velocity induced by droplet evaporation. In our experiments, with small droplets with contact-line radii of 0.8–1.0 mm and heights of about 0.3 mm and for slow flows (around 1 μm/sec), the Bond number is in a range of 0.03–0.04 and the capillary number is around 10^{-8}, so that the droplet shape can be regarded as a spherical cap.

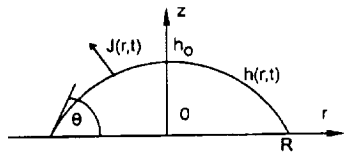

Figure 1. Droplet with the shape of a spherical cap rests on a flat surface. The contact angle is θ, the local height is $h(r,t)$, and the local evaporation flux is $J(r,t)$.

In Figure 1, a small drop of water on a glass surface, whose shape is that of a spherical cap, is presented. A cylindrical coordinate system is used with radial coordinate r and axial coordinate z. $S = \{h(r,t) | r \le R\}$ defines the surface of the droplet, where $h(r,t)$ is

$$h(r,t) = \sqrt{R^2/\sin^2\theta - r^2} - R/\tan(\theta) \tag{1}$$

where θ is the contact angle and R is the contact-line radius.

The volume of the droplet is

$$V(t) = \frac{\pi h(0,t)[3R^2 + h^2(0,t)]}{6} \tag{2}$$

where $h(0,t)$ is the droplet height as a function of time and R is the contact-line radius.

From eq 1, when we let $r = 0$, we have $h(0,t)$

$$h(0,t) = R \tan[\theta(t)/2] \tag{3}$$

Because water evaporates into the ambient air, the vapor concentration is distributed nonuniformly above the droplet. At the interface between the liquid and the vapor, the vapor concentration c is assumed to equal the saturation value c_v. Far above the droplet, the vapor concentration approaches an ambient value Hc_v (where H is the relative humidity of the ambient air). The difference in water vapor concentration $c_v(1 - H)$ drives the evaporation of water into the air, according to the diffusion equation

$$\frac{\partial c}{\partial t} = D\Delta c \tag{4}$$

where c is the local water vapor mass concentration and D is the vapor diffusivity. The boundary conditions are

$$\begin{aligned} &1.\ r < R,\ z = h(r):\ c = c_v \\ &2.\ r > R,\ z = 0:\ J = 0 \\ &3.\ r = \infty,\ z = \infty:\ c = H_v c_v \end{aligned} \tag{5}$$

Here J is the vapor mass flux that is due to evaporation.

The time required for the vapor-phase water concentration to adjust to changes in the droplet shape is of the order of R^2/D, where D is the diffusivity of the vapor in air and R is the contact-line radius. The ratio of this time to the droplet evaporation time t_f is $R^2/Dt_f \approx c_v(1 - H)/\rho$. In our experiments, we can take $H = 0.4$, $c_v = 2.32 \times 10^{-5}$ g/cm^3, and $\rho = 1$ g/cm^3, so that we obtain $R^2/Dt_f \approx c_v(1 - H)/\rho = 0.000\ 014 \ll 1$. Hence, the water vapor concentration adjusts rapidly compared to the time required for droplet evaporation, and the water evaporation can be considered to be at a quasi-steady state. We therefore neglect the transient term in eq 4 and obtain the

Laplace equation for the vapor concentration distribution:

$$\Delta c = 0 \tag{6}$$

As the droplet evaporates, the surface of the droplet descends toward the substrate. For this moving-boundary problem, we present a finite element method to solve eq 6 to calculate the vapor distribution above the droplet and the evaporation flux along the droplet surface.

At the air−liquid interface, the local evaporation flux $\vec{J}(r,t)$ is expressed as

$$\vec{J}(r,t) = D\vec{\nabla}c \tag{7}$$

The evaporation rate J_t over the whole surface is expressed by the following equation:

$$J_t = \int_{\Gamma_g} (\vec{J}\cdot\vec{n})\, d\Gamma_g \tag{8}$$

The above derivation assumes that the evaporation is not so rapid as to alter the droplet temperature enough to change the values of the parameters c_v or D.

2.2. Finite Element Method. We apply the FEM method to calculate the vapor concentration distribution above the droplet. For simplification, we describe all of the detailed derivations of FEM model in the Appendix. The final formulations of the FEM model are expressed by eqs A-5 to A-12. Incorporating the boundary conditions listed in eq 5, eqs A-5 to A-12 can be numerically solved to obtain the vapor concentration distribution.

3. Experimental Method

We use a microscopic particle tracer method to measure the rate of droplet evaporation. Figure 2 is a schematic of the imaging system used in our experiments to measure the droplet evaporation, with Figure 2b as an enlargement of element A in Figure 2a. A Nikon inverted fluorescence microscope (Eclipse, TE200) with a motorized X−Y stage (Prior, Inc.) is employed to locate the fluorescent particles. As shown in Figure 2b, a droplet of volume about 0.5 μL is deposited on a clean glass cover slip (Dow-Corning, No.1; 22 mm) and initially sealed by a cylindrical cap to block its evaporation (Once the droplet size and location have been precisely measured, the cap is removed and replaced by a cylinder open at the top to allow evaporation to begin while suppressing the effect of air currents on evaporation.) The glass cover slip with its holder is placed on the motorized X−Y stage. A 40× objective is coated with water, and the water coating is brought into contact with the cover slip, thus eliminating the air gap between the sample and the objective and to minimize the effect of refraction. Fluorescent particles 0.75 μm in diameter (Polyscience, Inc.) are used as tracers to map the droplet profiles at different times and thereby calculate the residual droplet volume. Particle images are detected by a CCD camera (PC-26C, Super Circuit Co.) with a resolution of 640 × 480 pixel. Then, the images are recorded onto a computer disk and analyzed by the SimplePCI image processing system (Compix, Inc.).

With the cylindrical cap in place to prevent evaporation, we move the X−Y stage around the perimeter of the droplet and measure the coordinates of the particles at the edge of the droplet. The coordinates of these particles are fitted by a circle so that the center and the radius of the droplet are determined. From the experimental results for about 500 droplets, we can conclude that the contact line of the droplet is indeed a circle and the radius of the contact line is about 850 ± 10 microns.

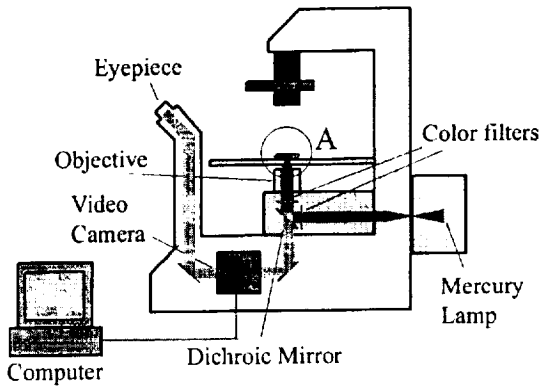

a

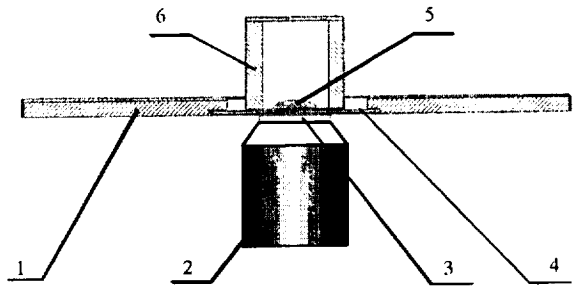

1.Glass coverslip holder 2.Fluorescence objective(40X)
3. Water 4.Glass coverslip 5. Droplet 6. Sealing cylinder cap

b

Figure 2. Experimental setup. Figure 2a is a Nikon fluorescence microscope, and Figure 2b is a blow-up of part A in Figure 2a.

We also obtained the residual droplet volume by measuring the droplet surface profiles at different times by finding the coordinates of fluorescent particles on the surface of the droplet. The results are shown in Figure 3, in which the symbols are the positions of fluorescence particles on the droplet surface and the line is a fit by a circular arc, representing a spherical cap. The standard error of the fit is about 1−2 micron. This implies the droplet shape is not affected by adding the tracer particles. The tracer particles might enhance pinning of the contact line, but it is hard to examine it. Because the droplet remains in the shape of a spherical cap at all times during droplet evaporation, we need only measure the height of the droplet as a function of time in order to reach an accurate measurement of the droplet surface and volume.

4. Results

4.1. Convergence of the FEM Computation. The convergence of the FEM computation is tested by systematically refining the mesh at the edge of the droplet according to the method described in Appendix A.4. The mesh near the edge of the droplet is refined several times over so that the number of

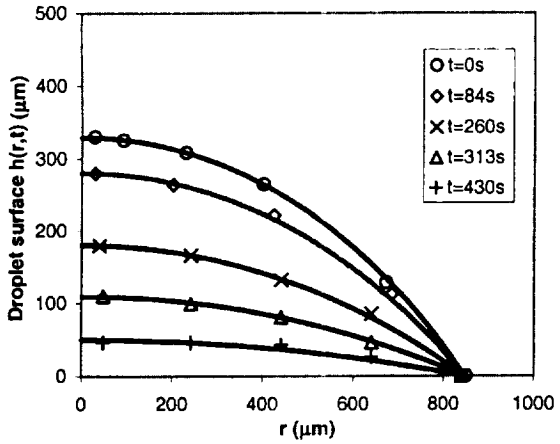

Figure 3. Measured droplet profiles at different times, for water evaporating from a droplet of initial radius $R = 0.85$ mm and height $h_0 = 0.329$ mm. The symbols show the locations of fluorescent particles on the droplet surface, and the lines are the fittings of circular arcs to these data. The fitting errors are about $1-2$ μm.

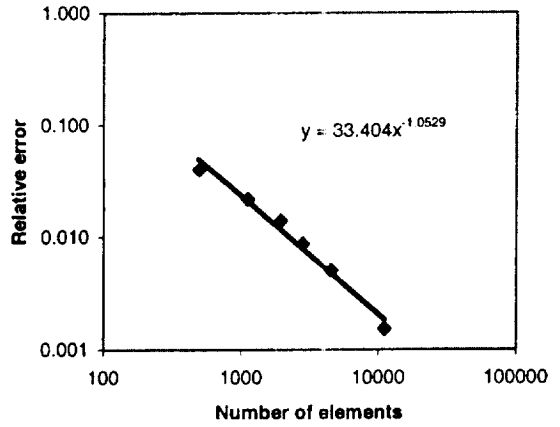

Figure 4. Relative error vs the number of FEM elements.

elements becomes large and the size of the elements near the edge becomes smaller. Subsequently, the evaporation flux and the total evaporation rate are calculated using eqs 7 and 8 for the different refined meshes. Numerical calculations show that as the number of the elements increases the total evaporation rate decreases for small numbers of elements and levels off when the number of elements exceeds about 5000. The relative error defined in eq A-13 is plotted in Figure 4, which shows that the relative error decreases linearly with the number of elements, as expected for linear shape functions. Figure 4 shows that when the number of elements in the circular sector is larger than 10 000 the relative error is small enough that the convergence criterion is satisfied. We can conclude that after the mesh has been locally refined 6-fold according to the method given in Appendix A.4, an acceptable FEM computational accuracy is attained. Using this protocol, the vapor concentration distribution, the evaporation rate, the height of the droplet, the contact angle, and the droplet volumes at different times are computed, as described in the following.

4.2. Vapor Concentration Distribution. When using the finite element model, eqs A-5 to A-12, to solve the vapor concentration distribution, we need to consider the boundary condition in eq 5, which is $c = Hc_v$ at $r,z \to \infty$. We impose this condition along a boundary at $(r^2 + z^2)^{1/2} = KR$, where K is a constant much larger than unity. By testing different values of

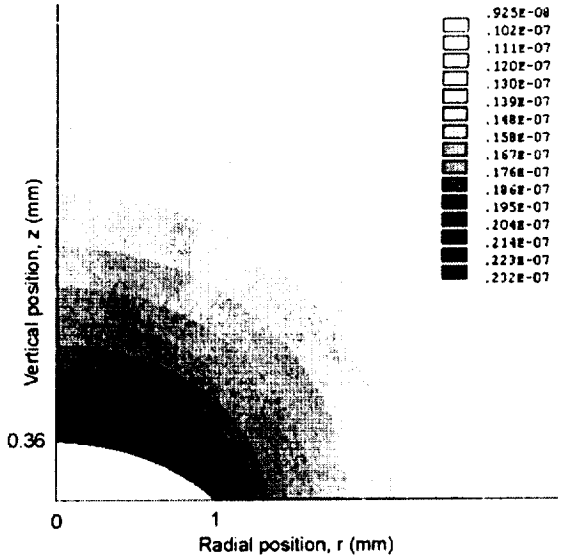

Figure 5. Contour plot of the vapor concentration distribution above a droplet of radius $R = 1$ mm and height $h_0 = 0.364$ mm. The parameters used in the FEM method are vapor diffusivity $D = 26.1$ mm^2/s, relative humidity $H = 0.40$ (i.e., 40%), and saturated vapor concentration on the droplet surface $c_v = 2.32 \times 10^{-8}$ g/mm^3, which is the value obtained form the CRC Handbook[16] at 25 °C. These parameter values are also used in Figures 6−10. The gray bars represent the vapor concentration in g/mm^3.

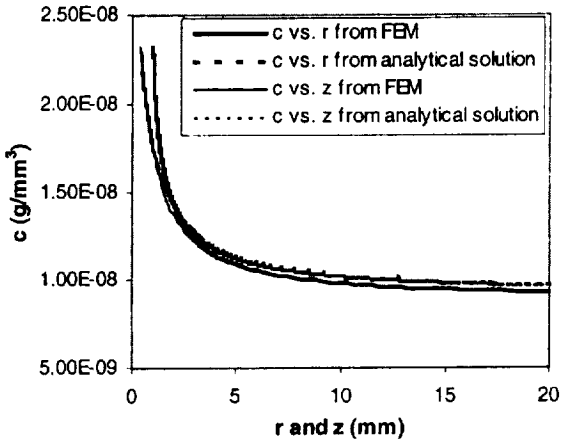

Figure 6. Vapor concentration distribution along the directions $z = 0$ and $r = 0$ from FEM (solid lines) and analytic solution (dashed lines). The FEM results along each direction superimpose on the analytic results.

K between 10 and 100, we find that the calculated vapor concentration at position $(r^2 + z^2)^{1/2} = 20R$ is close enough to the ambient vapor concentration c_∞ that the deviations are negligible; that is, $(c - c_\infty)/(c_v - c_\infty) < \epsilon \approx 0.002$. Therefore, in our FEM analysis, we use the boundary $(r^2 + z^2)^{1/2} = 20R$ to approximately represent $r,z \to \infty$.

The vapor concentration distributions at different times are then computed by the FEM method and presented in Figure 5. Figure 5 is a contour plot of the vapor concentration distribution when the droplet is starting to evaporate. The contour lines are concentrated near the droplet surface, where the vapor concentration has a large gradient. The vapor concentration along the lines $r = 0$ and $z = 0$ is plotted in Figure 6. When r and z are greater than $5R$, the changes in vapor concentration are small,

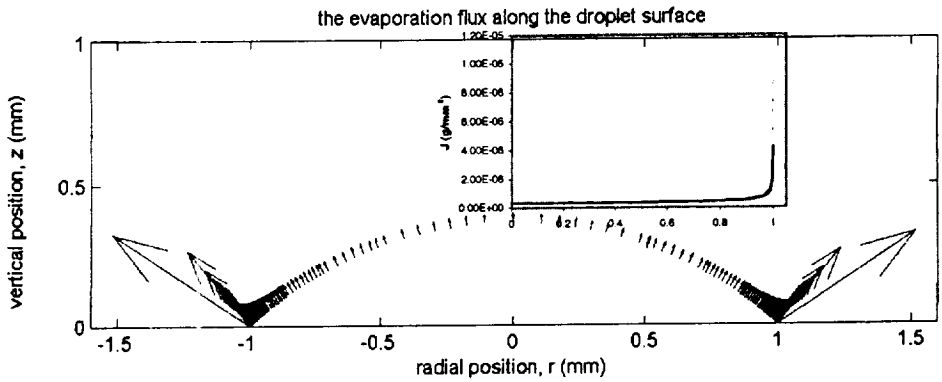

Figure 7. Evaporation flux along the droplet surface. The insert shows the magnitude of the evaporation flux along the droplet surface. The flux vector at the edge of the droplet does not orient along the normal direction, because when the mesh is refined several times near the edge of the droplet, the edge of the last element at $r = R$, which has become very small, does not perfectly match the droplet surface profile. This artifact is, however, confined to a single element and has negligible effect on the overall flux.

and the normalized vapor concentration, $(c - Hc_v)/(1 - H)c_v$, is so small, 0.02, that the cutoff, $(r^2 + z^2)^{1/2} = 20R$, is acceptable.

4.3. Vapor Flux above the Droplet. From the vapor concentration distribution, we calculate the vapor flux from eq 7. Along the droplet surface, the flux increases as one moves from the center top of the droplet to the contact line at the edge, where the flux is theoretically infinite, see Figure 7. The total evaporation rate can be evaluated from eq 8 by integrating along the droplet surface. The evaporation rate for a series of droplet shapes is used to compute the change in droplet volume vs time in the next section.

4.4. Droplet Volume, Height, and Contact Angle vs Time. By repeating the FEM analysis for a series of droplet heights, we simulate the droplet evaporation process. The radius and the initial height of the droplet are 1 and 0.364 mm. The parameters used in the FEM analysis are the vapor diffusivity $D = 26.1$ mm²/s (from *CRC Handbook of Chemistry and Physics*[16]), the relative humidity $H = 0.4$, and the saturated vapor concentration $c_v = 2.32 \times 10^{-8}$ g/mm³. A small time step of about $0.02t_f$ is used to calculate the time-dependent volume. At each time step, the loss of water is determined from the product of the total evaporation rate integrated over the droplet surface and the time step. As we described in section 2, the evaporation rate can be obtained from the vapor concentration distribution by using eqs 7 and 8 on the droplet surface. The new droplet volume is thereby calculated from the loss of the solvent and the previous droplet volume, and the new droplet surface profile can be derived from eq 2, for a spherical cap. This procedure is accurate, because the capillary number is low (Ca $\approx 10^{-8}$; so that the droplet remains a spherical cap), the contact line is pinned, and the vapor concentration field is quasi-steady; that is, it adjusts rapidly whenever the droplet shape changes. Thus, we can convert this moving-free-surface problem into a simple series of solutions to Laplace's equation. The height of the droplet and the contact angle decrease roughly linearly with time as shown in Figure 8, suggesting a nearly constant evaporation rate. The total evaporation rate, shown in the insert to Figure 8, is not quite constant; it decreases slightly during the droplet evaporation for an initial contact angle of 40°.

4.5. Experimental Results. In our experiments, we obtained the droplet evaporation rate by measuring droplet height at a series of times. Doing so is reliable because, as shown in Figure 3, the droplet shape remains a spherical cap during evaporation. From the height and the contact-line radius, the droplet volume at different times is calculated. The residual droplet volume vs

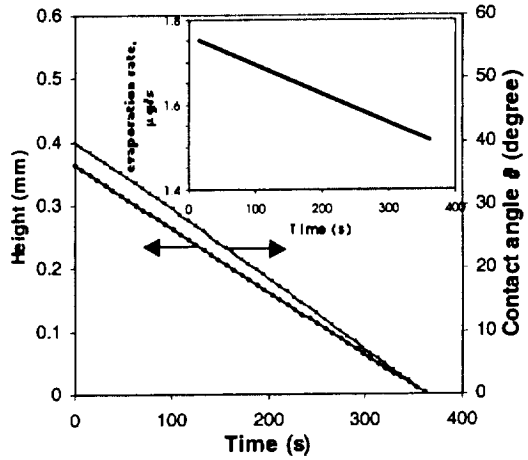

Figure 8. Height of the droplet and the contact angle vs time. The insert shows the evaporation rate vs time.

time is plotted in Figure 9 and compared with the results of the finite element simulation using the experimentally derived parameters. We can see that there is very good agreement between the experiment and the FEM calculations. The FEM results show that the evaporation rate changes slightly during evaporation as seen in Figure 8 and the solid line in Figure 9 is not a straight line. It changes its slope slightly during the initial drying process but has become almost constant near the end of drying.

In the experiments, we also measured the critical contact angle, the angle at which the contact line starts to recede for about 50 droplets, and obtained an average of 2−4°.

5. Discussion

5.1. Approximate Expression for the Evaporation Rate. The excellent agreement between the FEM computation and the experimental measurements confirms that the droplet evaporation is a quasi-steady-state process. This should be true whenever $R^2/Dt_f \approx c_v(1 - H)/\rho \approx c_v/\rho$ is small; that is, whenever the vapor phase has a density much smaller than that of the liquid, which is always true except near supercritical conditions. Thus, the quasisteady approximation for the vapor concentration field should be valid even for very rapidly evaporating droplets. It should be kept in mind, however, that for very rapidly evaporating droplets large temperature non-

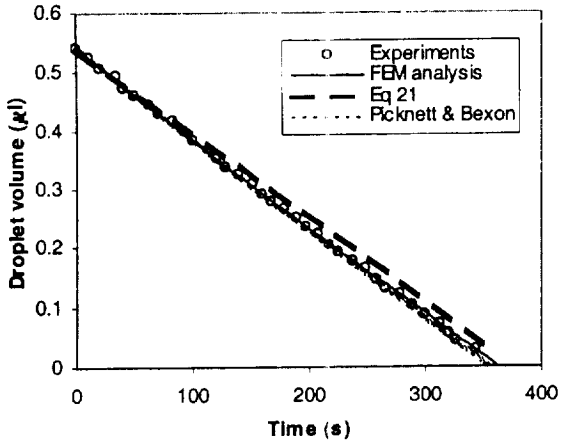

Figure 9. Symbols giving the residual droplet volume vs time calculated from the height of the droplet at different times and the contact-line radius. The thin solid line is the result of the FEM calculations, using the experimental conditions as parameters, i.e., $R = 0.95$ mm, $h_0 = 0.364$ mm, vapor diffusivity $D = 26.1$ mm^2/s, relative humidity $H = 0.38$ (i.e., 38%), and saturated vapor concentration on the droplet surface $c_v = 2.32 \times 10^{-8}$ g/mm^3 at temperature 25 °C. The dashed line is calculated by the approximate evaporation rate expression eq 21 using the same values of parameters as the FEM method. The thin dashed line is calculated by Picknett and Bexon's model[9] using the same value of parameters as the FEM method.

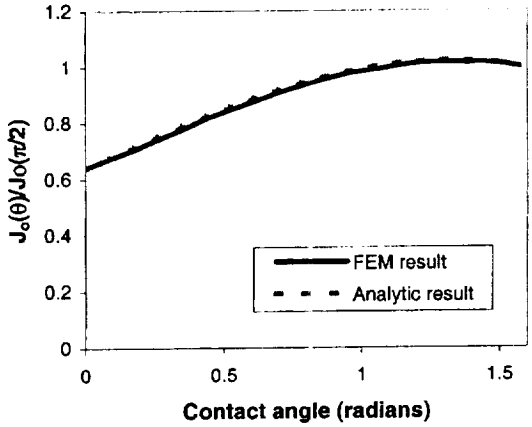

Figure 10. Ratio $J_0(\theta)/J_0(\pi/2)$ versus the contact angle. The solid line is calculated by FEM analysis, whereas the dashed line is from the analytical solution.

uniformities may develop because of latent heat and this will affect the evaporation flux.

The evaporation flux on the droplet surface calculated in our FEM analysis can be fitted by the following equation suggested by Deegan et al.:[13,14]

$$(\vec{J}\cdot\vec{n}) = J_0(1 - \tilde{r}^2)^{-\lambda} \tag{9}$$

where λ is a fitting parameter representing the nonuniformity of the evaporation flux on the droplet surface and $\tilde{r} \equiv r/R$. From fits of eq 9 to our FEM results, we obtain values of J_0 and λ for different contact angles, see Figures 10 and 11. Because Deegan et al. did not precisely define the relationships between J_0, λ, and the contact angle θ, we determine $J_0(\theta)$ and $\lambda(\theta)$ versus the contact angle empirically by using the finite element method. From Figure 10, we find that the ratio $J_0(\theta)/J_0(\pi/2)$ is close to unity when the contact angle θ is in a range of 70−90°

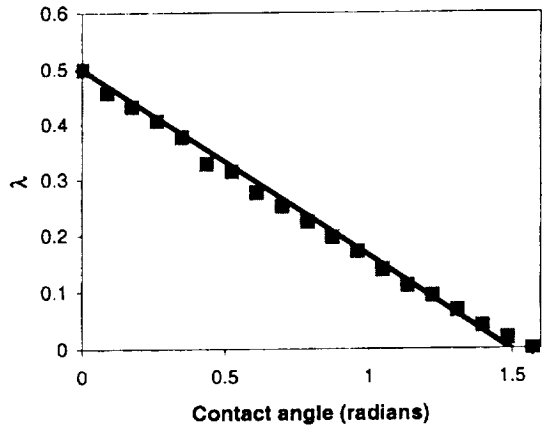

Figure 11. Evaporation rate exponent λ as a function of the contact angle, obtained by fitting eq 9 to the FEM results.

but starts to decrease linearly with θ for θ less than 60°. At $\theta = 0°$, the ratio reaches the value of 0.6377. The error between the FEM result and the exact solution shown by the dashed line in Figure 10 is less than 1.5%. Surprisingly, Figure 11 shows that λ decreases linearly with θ over the range of 0−90°, and so λ can be expressed by a simple linear function, $\lambda(\theta) = 0.5 - \theta/\pi$, which is different from a result cited by Deegan et al., $\lambda(\theta) = (\pi - 2\theta)/(2\pi - 2\theta)$. However, this latter formula for $\lambda(\theta)$ applies to the equation $J(r) \sim (1 - \tilde{r})^{-\lambda}$ and not to the equation used here (and by Deegan et al.), namely, $J(r) \sim (1 - \tilde{r}^2)^{-\lambda}$. Obviously, the formula for the exponent $\lambda(\theta)$ will differ for these two expressions. By using the formula $\lambda(\theta) = 0.5 - \theta/\pi$, the largest relative error between the prediction from eq 9 and the results from the FEM analysis over the range of 0−90° is less than 6%, and this value decreases toward zero as the contact angle approaches either 0° or 90°. From Figures 10 and 11, we conclude that the evaporation rate is a function of the contact angle θ. Using eq 9, the evaporation rate becomes

$$-\dot{m}(t) = \int_S (\vec{J}(r,t)\cdot\vec{n})\, dS = \int_0^1 2\pi\, \tilde{r}\cdot R^2\cdot \vec{J}_0(\theta)(1 - \tilde{r}^2)^{-\lambda(\theta)} \sqrt{\left(\frac{\partial h(r,t)}{\partial r}\right)^2 + 1}\, d\tilde{r} \tag{10}$$

where S is the area of integration and $\partial h(r,t)/\partial r$ is the derivative of $h(r,t)$ with respect to r, given for a spherical cap by

$$\frac{\partial h(r,t)}{\partial r} = \frac{-\tilde{r}}{\sqrt{1/\sin^2\theta - \tilde{r}^2}} \tag{11}$$

We find that the term $[(\partial h(r, t)/\partial r)^2 + 1]^{1/2}$ in the integration kernel in eq 10 can be approximated by

$$\sqrt{\left(\frac{\partial h(r,t)}{\partial r}\right)^2 + 1} = (1 - \sin^2\theta\, \tilde{r}^2)^{-0.5} \cong (1 - \tilde{r}^2)^{-\delta(\theta)} \tag{12}$$

where $\delta(\theta)$ is an empirical function of contact angle θ. Inserting eq 12 into eq 10, we have

$$-\dot{m}(t) = \int_0^1 2\pi\, \tilde{r}\cdot R^2\cdot J_0(\theta)(1 - \tilde{r}^2)^{-\Lambda(\theta)}\, d\tilde{r} \tag{13}$$

where $\Lambda(\theta) = \lambda(\theta) + \delta(\theta)$ is a combination of two factors, one is a parameter reflecting the nonuniformity of the evaporation flux and the other reflects the droplet surface area per unit area of substrate at each value of $\tilde{r}$. When the contact angle is

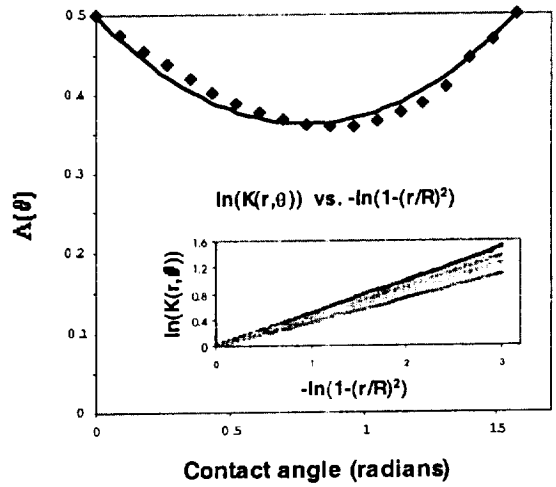

Figure 12. $\Lambda(\theta)$ versus the contact angle θ. The solid symbols are the slopes of the curves in the insert obtained by fitting $\ln[K(r,\theta)] = \ln\{(1-\bar{r}^2)^{-\lambda(\theta)}[(\partial h(r,\theta)/\partial r)^2+1]^{1/2}\}$ with $-\Lambda(\theta)\ln(1-\bar{r}^2)$. The line is a parabola, eq 14, fitted to the solid points.

90°, because $\lambda(\pi/2)$ is 0 and $\delta(\pi/2)$ is 0.5, $\Lambda(\pi/2)$ equals 0.5. When the contact angle is 0°, because $\lambda(0)$ is 0.5 and $\delta(0)$ is 0, $\Lambda(0)$ also equals 0.5. Using the results of our FEM analysis, we fit the term $(1-\bar{r}^2)^{-\lambda(\theta)}[(\partial h(r,t)/\partial r)^2+1]^{1/2}$ in eq 10 with the equation $(1-\bar{r}^2)^{-\Lambda(\theta)}$ at a given contact angle to obtain $\Lambda(\theta)$ and plot this in Figure 12 as solid diamonds. In the insert to Figure 12, we plot the term $\ln[K(r,\theta)] = \ln\{(1-\bar{r}^2)^{-\lambda(\theta)}\cdot[(\partial h(r,\theta)/\partial r)^2+1]^{1/2}\}$ against $-\ln(1-\bar{r}^2)$, and the slopes of the lines give $\Lambda(\theta)$. The points in Figure 12 can be fitted well by a parabola, namely,

$$\Lambda(\theta) = 0.2239(\theta - \pi/4)^2 + 0.3619 \qquad (14)$$

where θ is given in radians.

Substituting eq 14 into eq 13, and integrating, gives

$$-\dot{m}(t) = \frac{\pi R^2 J_0(\theta)}{1-\Lambda(\theta)} = \frac{\pi R^2 J_0(\theta)}{1-(0.2239(\theta-\pi/4)^2+0.3619)} \qquad (15)$$

Equation 15 is a general formula for the droplet evaporation rate for any contact angle ($0° < \theta < 90°$). In eq 15, we note that $J_0(\theta)$, the evaporation flux at the center of the droplet, is also a function of the contact angle θ, as shown in Figure 10. To simplify eq 15, we calculated the ratio of $J_0(\theta)/J_0(\pi/2)(1-\Lambda(\theta))$ using the FEM results and plot this in Figure 13, which is given by solid squares. In Figure 13, the line is obtained from the fitting function

$$\frac{J_0(\theta)}{1-\Lambda(\theta)} = J_0(\pi/2)(0.27\theta^2 + 1.30) \qquad (16)$$

where θ is given in radians. The results predicted by eq 16 are compared to the exact solution for contact angle ranging from 0 to 90°, and the largest error is less than 6%.

Substituting eq 16 into eq 15, we derive an approximate expression for the droplet evaporation rate at any contact angle ($0° < \theta < 90°$), which is

$$-\dot{m}(t) = \pi R^2 J_0(\pi/2)(0.27\theta^2 + 1.30) \qquad (17)$$

where $J_0(\pi/2)$ is the evaporation flux for the contact angle 90°.

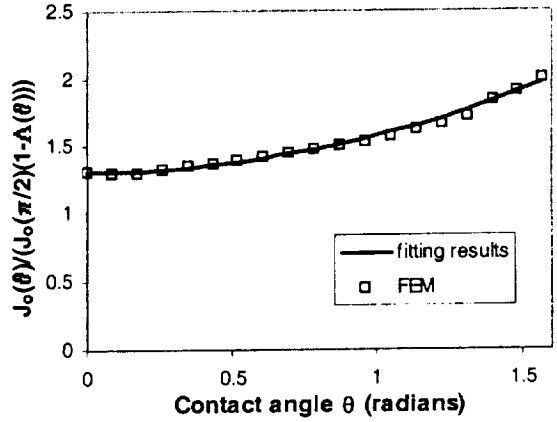

Figure 13. Ratio $J_0(\theta)/J_0(\pi/2)(1-\Lambda(\theta))$ versus the contact angle, calculated from Figures 10 and 12.

For $\theta = 90°$, the evaporation flux is uniform everywhere along the droplet surface. The solution of eq 6 for a contact angle of 90° is, by symmetry, the same as the solution for a droplet suspended in the air without the presence of a substrate. For a suspended droplet, the boundary conditions are $(r^2+z^2)^{1/2} = R$:$c = c_v$ and $(r^2+z^2)^{1/2} = \infty$:$c = Hc_v$, and we derive the evaporation flux $J_0(\pi/2)$ from eq 7, which is

$$J_0(\pi/2) = \frac{D(1-H)c_v}{R} \qquad (18)$$

Combining eqs 17 and 18 gives

$$-\dot{m}(t) = \pi RD(1-H)c_v(0.27\theta^2 + 1.30) \qquad (19)$$

From eq 19, we can see that at a given contact angle the evaporation rate is proportional to the contact-line radius R, the vapor concentration difference $(1-H)c_v$, and the diffusivity D and depends weakly on the contact angle θ. Figure 13 shows that when the contact angle is less than 40° (0.7 rad) the dependence on θ almost becomes flat, and therefore, the evaporation rate is almost constant. Equation 19 agrees well with the theoretical results obtained by Picknett and Bexon.[10] We calculate the evaporation rate as a function of the contact angle according to eq 19 and compare the result to that derived by Picknett and Bexon. The averaged relative error between the two predictions is less than 1%. However, eq 19 is different from the prediction of the model presented by Bourges and Shanahan.[6] When the contact angle θ is close to 0°, their model predicts an evaporation rate of 0, which is incorrect. This is because that Bourges and Shanahan assume that the vapor concentration gradient is uniform along the surface of the sessile droplet and is set by the radius of curvature of the droplet surface, which becomes infinite when the droplet becomes flat, leading to zero evaporation flux. Actually, from our FEM results, Figure 7, we can see the concentration gradient along the surface of a sessile droplet is not uniform compared to the uniform concentration gradient on the surface of a spherical droplet.

Equation 19 gives the exact solution for two limiting cases, for a contact angle of 0° and a contact angle of 90°. When the contact angle is close to 90°, eq 19 gives

$$-\dot{m}(t) = 2\pi D(1-H)c_v R \qquad (20)$$

whereas when the contact angle θ is close to 0°, eq 19 gives

$$-\dot{m}(t) = 4D(1 - H)c_v R \tag{21}$$

Both eqs 20 and 21 are consistent with the results of Picknett and Bexon[10] for the two cases of the contact angles, 90 and 0°, respectively.

We use eq 21 to calculate the droplet volume vs time and compare this with the results from the FEM method and the experimental measurement as shown in Figure 9. Figure 9 shows that the results calculated by eq 21 are consistent with those from the FEM method, Picknett and Bexon's model, and the experiments. The relative error between eq 21 and the experiments is 3.6%. This implies that when the initial contact angle is less than 40° the evaporation rate can be approximated by eq 21 and the evaporation rate can be regarded as a constant. The prediction from the FEM analysis, which is the thin solid line, is very close to the prediction of Picknett and Bexon's model, which is the thin dashed line. The relative error in the drying times predicted by FEM and the theoretical model of Picknett and Bexon is less than 1.3%.

5.2. Comparison with the Exact Solution. Deegan et al.[14] reported an analytical solution for the Laplace equation, which was derived by Lebedev.[9] Lebedev considered a charged surface formed by the union of two spherical domains, and derived the electrostatic potential distribution in the space exterior to this surface by using toroidal coordinates. In toroidal coordinates, the potential distribution is given by

$$u = V\sqrt{2\cosh\alpha - 2\cos\beta}\int_0^\infty \frac{\cosh[(\pi - \beta_1)\tau]\sinh[(\beta - \beta_2)\tau] + \cosh[(\pi - \beta_2)\tau]\sinh[(2\pi + \beta_1 - \beta)\tau]}{\cosh(\pi\tau)\sinh[(2\pi + \beta_1 - \beta_2)\tau]} P_{-(1/2)+i\tau}(\cosh\alpha)\,d\tau \tag{22}$$

where α and β are the toroidal coordinates, V is the potential on the surface, and β_1 and β_2 are two angles of $\pi - \theta$ and $\pi + \theta$, $P_{-(1/2)+i\tau}(\cosh\alpha)$ is the Legendre function of the first kind and is expressed by

$$P_{-(1/2)+i\tau}(\cosh\alpha) = \frac{2}{\pi}\coth(\pi\tau)\int_\alpha^\infty \frac{\sin(\tau t)}{\sqrt{2\cosh t - 2\cosh\alpha}}\,dt \tag{23}$$

Although eq 22 has a different form from Picknett and Bexon's solution, they are identical because they are derived from the same model.

The toroidal coordinates α and β are related to the cylindrical coordinates r and z by

$$r = \frac{R\sinh\alpha}{\cosh\alpha - \cos\beta} \tag{24}$$

$$z = \frac{R\sin\beta}{\cosh\alpha - \cos\beta} \tag{25}$$

where R is the contact-line radius.

The electrostatic potential around a lens-shaped object with uniform surface potential and the vapor concentration distributions above an evaporating droplet are equivalent, because they are both solutions of the Laplace equation. By symmetry, the solution to Laplace's equation in the half-plane above a spherical cap is identical to that of a lens-like shape formed from two back-to-back spherical caps. Thus, we can apply the solution of the electrostatic potential in toroidal coordinates for a lens-like shape to the vapor concentration distribution above the droplet. We consider the electrostatic potential u as a dimensionless vapor concentration, $u = (c - c_\infty)/(c_v - c_\infty)$, where c_v and c_∞ are the vapor concentration on the droplet surface and in the ambient, respectively. Then $u = 1$ on the droplet surface. For the lens-like geometry, we let $\beta_1 = \pi - \theta$ and $\beta_2 = \pi + \theta$, where θ is the contact angle. From eq 25, we obtain the vapor concentration distribution

$$\frac{c - c_\infty}{c_v - c_\infty} = \sqrt{2\cosh\alpha - 2\cos\beta}\int_0^\infty \frac{\cosh(\theta\tau)}{\cosh(\pi\tau)}\frac{\cosh[(2\pi - \beta)\tau]}{\cosh[(\pi - \theta)\tau]} P_{-(1/2)+i\tau}(\cosh\alpha)\,d\tau \tag{26}$$

Once the vapor concentration is known, from eq 7, we can obtain the evaporation flux distribution along the droplet surface, which in toroidal coordinates is

$$(\vec{J}\cdot\vec{n}) = -\frac{D(\cosh\alpha - \cos\beta)}{R}\frac{\partial u}{\partial\beta}\Big|_{\beta=3\pi-\theta} \tag{27}$$

Inserting eq 26 into eq 27, the evaporation flux is

$$(\vec{J}\cdot\vec{n}) = -\frac{D(c_v - c_\infty)}{R}\left[\frac{\sin\theta}{2} + (\cosh\alpha + \cos\theta)^{(3/2)}\int_0^\infty \frac{\cosh(\theta\tau)}{\cosh(\pi\tau)}\tanh[(\pi - \theta)\tau]\tau P_{-(1/2)+i\tau}(\cosh\alpha)\,d\tau\right] \tag{28}$$

which corrects eq A2 of Deegan et al.[14]

Eqs 6 and 28 are the expressions for the vapor concentration distribution above the droplet and the evaporation flux along the droplet surface, respectively. Both of them have complicated integrations, so closed forms are not available. A numerical method is therefore used to solve these two formulas.

Now we evaluate eqs 26 and 28 for two special cases, $\theta = 0$ and 90°. For the case of $\theta = 90°$, eq 26 becomes

$$\frac{c - c_\infty}{c_v - c_\infty} = \sqrt{\frac{\cosh\alpha - \cos\beta}{\cosh\alpha + \cos\beta}} = \frac{R}{r'} \tag{29}$$

where $r' \equiv (r^2 + z^2)^{1/2}$

Equation 29 becomes

$$(\vec{J}\cdot\vec{n}) = \frac{D(c_v - c_\infty)}{R} \tag{30}$$

Equations 9 and 30 are consistent with the results obtained by solving the Laplace equation in cylindrical coordinates. Inserting eq 30 into eq 10, the evaporation rate obtained is identical to eq 20.

For the case of $\theta = 0°$, eqs 26 and 28 can be solved:

$$\frac{c - c_\infty}{c_v - c_\infty} = \frac{3}{2} + \frac{1}{\pi}\arctan\left[\frac{\cos\beta - \sinh^2\left(\frac{\alpha}{2}\right)}{\cos\left(\frac{\beta}{2}\right)\sqrt{2\cosh\alpha - 2\cos\beta}}\right] \tag{31}$$

$$(\vec{J}\cdot\vec{n}) = \frac{D(c_v - c_\infty)}{R}\frac{2}{\pi}\cosh\left(\frac{\alpha}{2}\right) \tag{32}$$

In cylindrical coordinates, eq 32 becomes

$$(\vec{J}\cdot\vec{n}) = \frac{D(c_v - c_\infty)}{R}\frac{2}{\pi}(1 - \tilde{r}^2)^{-0.5} \tag{33}$$

Equation 33 implies that the fitting parameter λ in eq 9 becomes 0.5 when the contact angle reaches the limiting value of 0°. From eqs 30 and 33, we find the ratio $J_0(0)/J_0(\pi/2) = [(2/\pi)(D(c_v - c_\infty)/R)]/(D(c_v - c_\infty)/R) = 2/\pi$. The ratio from Figure 10 computed by the FEM method for $\theta = 0$ is 0.6377, which is indeed very close to the value $2/\pi = 0.6366$.

Substituting eq 33 into eq 10, we also rederive the same evaporation rate for $\theta = 0°$ given by eq 21.

We can now compare the FEM results with the analytical results obtained by solving eqs 26 and 27. In Figure 6, the vapor concentration distributions along the $r = 0$ and $z = 0$ directions calculated by FEM are indistinguishable from the results obtained from eq 26. Figure 10 shows that the ratio $J_0(\theta)/J_0(\pi/2)$ computed by FEM and from the analytical solution are nearly identical.

We note that the analytic solution is only available for the special case of a spherical cap, which is valid for small droplets ($R \leq 1$ mm). For larger droplets, the bond number exceeds 0.1, and gravitational sag becomes important. The analytic solution also fails when the evaporation rate is fast enough to change the temperature of the droplet enough to affect the saturated vapor concentration c_v. In the case of gravitational sag, eq 1 for the droplet surface profile must be replaced by an ordinary differential equation for the static droplet shape under the influence of gravity and surface tension, which must be solved each time step. If temperature variations become large, the temperature field inside the droplet must be obtained each time step by solving a quasisteady heat equation (as is done in a forthcoming paper[15]). In both cases, however, the most important simplifications of our approach remain valid: the vapor concentration field is at quasi-steady-state (because $R^2/Dt_f = c_v(1 - H)/\rho$ is small), and the droplet shape is at static equilibrium (because $Ca = \mu\bar{u}_r/\sigma$ is small). Thus, the simple quasi-steady-state FEM method presented here remains accurate for a very wide range of conditions, including conditions for which eq 26, the electrostatic solution, does not apply, such as when the droplet is not a spherical cap (because of gravity) or the temperature is not uniform within the droplet because of rapid evaporation.

5.3. Comparison of Model Predictions with Other Experimental Results. We now compare the results calculated from the simple empirical formula eq 19 (which fits the FEM and analytic results almost perfectly) with the experimental results reported by Birdi et al.[3] and Rowan et al.[7] Birdi et al.[3] studied the evaporation of droplets of water on glass by weighing the residual droplet mass. In general, we should use eq 19 to compare with their experiments, but this equation is well approximated by eq 21 when the initial contact angle θ is les than 40°, as is the case in these experiments. Their paper does not give the parameters D, H, and c_v. Therefore, we obtain the experimental term $4D(1 - H)c_v$ from one of their experiments and then apply this constant to calculate the results for other droplets with different contact line radii. The results are plotted in Figure 14, which shows that if we arbitrarily fit the set of experimental data for the droplet with contact-line radius of 2.01 mm by eq 21 we obtain the fitting constant $4D(1 - H)c_v = 6.5 \times 10^{-5}$ g s^{-1} mm^{-1} with correlation coefficient $R = 0.9999$. With this constant, the residual masses of the droplets of radii 2.53 and 2.93 mm are calculated by the integration of eq 21 with time. The results are plotted in Figure 14, in which the solid lines are the calculated results, which are very close to the experimental results. The average relative errors between the theoretical predictions and the experiments are 3.1% and 3.5% for droplet radii 2.53 and 2.93 mm, respectively.

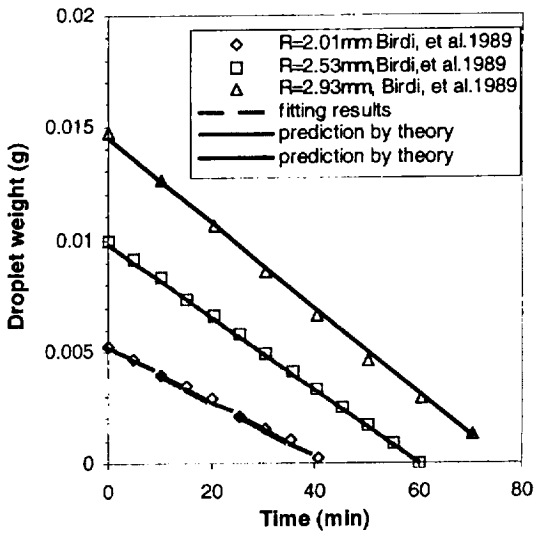

Figure 14. Comparison of the time-dependent weight from the model predictions (eq 21) and the results published by Birdi et al.[3] for droplets of water of radii 2.01, 2.53, and 2.93 mm on glass at $T = 22$ °C. The theory for $R = 2.01$ mm was fit to the data by adjusting $4D(1 - H)c_v$ to the best-fit value of 0.000 065 g mm^{-1} s^{-1}, and this was held fixed for the other experiments. The symbols are experimental results and the lines are the model predictions.

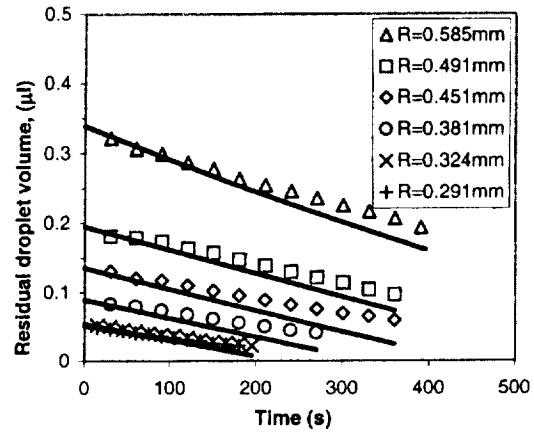

Figure 15. Comparison between the model prediction (eq 19) and the results published by Rowan et al.[7] for water droplets with radii $R = 0.585$, 0.491, 0.451, 0.381, 0.324, and 0.293 mm on PMMA substrates at $T = 21.5$ °C. All parameters in eq 19 are obtained from Rowan's paper, and they are vapor-phase water diffusivity $D = 17$ mm^2/s, relative humidity $H = 0.55$ (i.e., 55%), and saturated vapor concentration on the droplet surface $c_v = 1.9 \times 10^{-8}$ g/mm^3. The symbols are the experimental results, and the lines are the model predictions.

We also compare our model's predictions with Rowan's[7] results in Figure 15. Rowan et al. studied the height and the contact angle as functions of time for a water droplet on a PMMA substrate by using a Krüss contact-angle meter. In their experiments, the droplets have an initial contact angle of about 80°. Therefore, we employ eq 19 to calculate the residual droplet volume versus time. Here, the parameters in eq 19 are directly obtained form Rowan's paper. They reported that the water vapor diffusivity is $D = 17$ mm^2/s (which is a fitting value by using their model to their experimental results), the relative humidity is $H = 0.55$ (i.e. 55%), and the saturated vapor concentration on the droplet surface is $c_v = 1.9 \times 10^{-8}$ g/mm^3. The contact line radii for six different droplets are 0.585, 0.491,

0.451, 0.381, 0.324, and 0.293 mm. From Figure 15, we can see that, when droplet is bigger (R = 0.585 and 0.491 mm), our model predicts the experimental results fairly well, and the average relative errors between the predictions and the experiments are 7.4% and 9.7%, respectively. As the droplet size becomes smaller, the relative errors between the model prediction and the experiments become larger and are in the range of 10−25%. It is nearly impossible that evaporation cooling produces such big errors because in the forthcoming paper[15] we have calculated that the temperature drops in the droplet are only about 0.02 °C, which has hardly any effects on c_v and D. Possible reasons for the errors are that when droplet size is smaller (below 0.451 mm) the contact angle of the droplet is hard to determine precisely by the method described in the paper or that the humidity used here is not the true value.

In all of these cases, the overall evaporation rate remains nearly constant as the droplet dries out, and thus, the singularity in evaporation flux at the droplet edge is of little consequence for the overall rate of droplet drying. However, this singularity in evaporation flux creates a droplet flow field with a singularity at the contact line. In addition, small temperature variations along the droplet surface, which have negligible effects on the drying rate, induce Marangoni stresses (Scriven[17]), which affect qualitatively the flow inside the droplet. In our forthcoming paper,[15] this flow field will be examined both theoretically and experimentally.

6. Conclusion

An FEM model is developed to solve the vapor concentration distribution and the evaporation flux above a droplet that is small enough that its shape is not influenced by gravity and is therefore a spherical cap. The vapor phase water concentration field adjusts rapidly to changes in droplet height and can be regarded as quasisteady. The evaporation flux along the droplet surface is not uniform and becomes singular at the edge of the droplet and can be fitted by the expression $J_0(\theta)(1 - (r/R)^2)^{-\lambda(\theta)}$ suggested by Deegan and co-workers, where r is the radial position along the droplet, R is the droplet radius, and $J_0(\theta)$ and $\lambda(\theta)$ are empirical functions of the contact angle θ, which give the precise predictions comparing to the results obtained by Deegan and co-workers.[14] Neglecting the nonuniformity of the evaporation flux along droplet surface will lead an inaccurate theoretical result. FEM results also show that the overall evaporation rate is almost constant over the whole evaporation period when the initial contact angle is less than 40°. The FEM results agree well with the experimental measurements. Finally, for contact angles between 0 and 90°, an accurate approximate expression for the evaporation rate is presented: $-\dot{m}(t) = -\pi RD(1 - H)c_v(0.27\theta^2 + 1.30)$, where D is the gas-phase diffusivity, H is the relative humidity, θ is the contact angle in radians, and $m(t)$ is the time-dependent droplet mass. This equation is confirmed by Picknett and Bexon's results. For $\theta < 40°$, this expression can be reduced to just $-\dot{m}(t) = 4RD(1 - H)c_v$. The results predicted by this model compare very well with literature data without parameter fitting. The FEM results are also confirmed by an analytical formula derived by Lebedev[9] for the electrostatic potential produced by a charged lens and by the theoretical solution of Picknett and Bexon.[10]

Acknowledgment. We thank NASA Microgravity Research Division for supporting this study through Grant NAG3-2134.

Appendix

We here derive the FEM element model that is used to calculate the vapor concentration distribution.

A.1. Weak Formulation. From a variational analysis, the weak form of eq 6 in the cylindrical coordinate system is

$$\int_\Omega w(\bar{\nabla}\cdot(Dr\bar{\nabla}c))\,d\Omega = 0 \tag{A-1}$$

where Ω is the domain of the vapor phase, which is the semiinfinite half plane above the droplet excluding the droplet volume, and w is the weighting function. Integrating eq A-1 by parts gives

$$\int_\Omega \bar{\nabla}w\cdot(Dr\bar{\nabla}c)\,d\Omega - \int_{\Gamma_h}(rD\bar{\nabla}c)\cdot\vec{n}\,d\Gamma = 0 \tag{A-2}$$

The second term in eq A-2 is an integration over the boundary Γ, where $\Gamma = \Gamma_g + \Gamma_h$, and $\Gamma_g \cap \Gamma_h = \varnothing$, and $\vec{n}$ is the outward-pointing unit vector along the surface. Γ_g is the droplet free surface, and Γ_h is the dry substrate surface excluding the area on which the droplet rests. Boundary condition 1 in eq 5 applies along Γ_g, and boundary condition 2 applies along Γ_h. The properties of the weighting function w are as follows: along $\Gamma = \Gamma_g$, $w = 0$; along $\Gamma = \Gamma_h$, $w = 1$, which we have used to derive eq A-2.

A.2. Galerkin Method. To complete the finite element model, we apply the Galerkin method to approximate the concentration c and the weighting function w:

$$c = \sum_{A=1}^{n} d_A N_A \tag{A-3}$$

$$w = \sum_{A=1}^{n} x_A N_A \tag{A-4}$$

d_A and x_A are the coefficients on node A, n is the total number of nodes, and N_A is shape function for node A.

When eqs A-2, A-3, and A-4 are combined, the finite element model discretization of eq 6 is obtained as follow:

$$\mathbf{KD} = \mathbf{F} \tag{A-5}$$

In this equation, **K**, **F**, and **D** are

$$\mathbf{K} = [k_{AB}] = [\int_\Omega \bar{\nabla}N_A\cdot\bar{\nabla}N_B r\,d\Omega] \tag{A-6}$$

$$\mathbf{F} = [f_A] = [\int_\Gamma \bar{\nabla}N_A\cdot\vec{n}\,r\,d\Gamma] \tag{A-7}$$

$$\mathbf{D} = [d_A] = [d_1, d_2, d_3, \cdots, d_A]^T \tag{A-8}$$

A.3. Shape Function. We employ linear triangular elements in the finite element model, eqs A-6 to A-8. The shape functions are

$$N_1 = L_1 \tag{A-9}$$

$$N_2 = L_2 \tag{A-10}$$

$$N_3 = L_3 \tag{A-11}$$

$$L_1 + L_2 + L_3 = 1 \tag{A-12}$$

L_1, L_2, and L_3 are the local variables in each triangular element, and only two of them are independent variables, as specified by eq A-12.

A.4. Convergence Criteria and Mesh Refinement. Because two kinds of boundary conditions meet at the edge of the droplet, the evaporation flux becomes singular there. To overcome this

difficulty, we refine the mesh near the edge of the droplet. For convenience, we use a commercial software package, Ansys 5.6, to generate the mesh for our FEM analysis. Initially, the mesh is generated coarsely, and the FEM code is then used to calculate the vapor concentration and the evaporation rate. Next, we choose a circular sector with a radius of $r_1 = 0.5R$ centered at the edge of the droplet in the initial mesh and refine all of the elements in this area. The vapor concentration and the evaporation rate are calculated again for the new mesh. We compare the current total evaporation rate $J_{t,i}$ on mesh refinement i to $J_{t,i-1}$, which is for the less refined mesh $i-1$, to see whether they satisfy the following criteria:

$$\epsilon = \frac{|J_{t,i} - J_{t,i-1}|}{J_{t,i}} < 0.005 \qquad \text{(A-13)}$$

where J_t is expressed by eq 8

$$J_t = \int_{\Gamma_g} (\vec{J}\cdot\vec{n})\, d\Gamma_g \qquad \text{(A-14)}$$

To obtain an accurate vapor concentration distribution, the mesh near the edge of the droplet is refined continuously until the criterion in eq A-13 is satisfied. However, the new, ith, refinement is concentrated in a circular sector with radius $r_i = 0.68r_{i-1}$, where r_{i-1} is the radius of the circular sector used in the r_{i-1}th refinement. The final refined mesh, after six iterated refinements, has 11071 elements in the circular sector.

References and Notes

(1) Jing, J. P.; Reed, J.; Huang, J.; Hu, X.; Clarke, V.; Edington, J.; Housman, D.; Anantharaman, T. S.; Huff, E. J.; Mishra, B.; Porter, B.; Shenkeer, A.; Wolfson, E.; Hiort, C.; Kantor, R.; Aston, C.; Schwartz, D. C. *Proc. Natl. Acad. Sci. U.S.A.* **1998**, *95*, 8046.
(2) Li, L.; Hu, H.; Larson, R. G. To be submitted, 2001.
(3) Birdi, K. S.; Vu, D. T.; Winter, A. *J. Phys. Chem.* **1989**, *93*, 3702.
(4) Birdi, K. S.; Vu, D. T. *J. Adhes. Sci. Technol.* **1993**, *7*, 485.
(5) Shanahan, M. E. R.; Bourges, C. *Int. J. Adhes. Adhes.* **1994**, *14*, 201.
(6) Bourges, C.; Shanahan, M. E. R. *Langmuir* **1995**, *11*, 2820.
(7) Rowan, S. M.; McHale, G.; Newton, M. I. *J. Phys. Chem. B* **1995**, *99*, 13268.
(8) Rowan, S. M.; McHale, G.; Newton, M. I.; Toorneman, M. *J. Phys. Chem. B* **1997**, *101*, 1265.
(9) Lebedev, N. N. *Special Functions and Their Application*; Prentice-Hall: Englewood Cliffs, New Jersey, 1965.
(10) Picknett, R. G.; Bexon, R. *J. Colloid Interface Sci.* **1977**, *61*, 336.
(11) Erbil, H. Y.; Meric, R. A. *J. Phys. Chem. B* **1997**, *101*, 6867.
(12) Meric, R. A.; Erbil, H. Y. *Langmuir* **1998**, *14*, 1915.
(13) Deegan, R. D.; Bakajin, O.; Dupont, T. F.; et al. *Nature* **1997**, *389*, 827.
(14) Deegan, R. D.; Bakajin, O.; Dupont, T. F.; et al. *Phys. Rev. E* **2000**, *62*, 756.
(15) Hu, H.; Larson, R. G. *Phys. Fluids* **2001**, to be submitted.
(16) Weast, R. C.; Astle, M. J. *CRC Handbook of Chemistry and Physics*, 62nd ed.; CRC Press: Boca Raton, FL, 1981−1982.
(17) Scriven, L. E. *Chem. Eng. Sci.* **1960**, *12*, 98−108.